A&A, 686, A102 (2024)
https://doi.org/10.1051/0004-6361/202449434

Astronomy & Astrophysics

Sublimation of volatiles from H_2O:CO_2 bulk ices in the context of comet 67P/Churyumov-Gerasimenko

I. N_2 and CO

K. A. Kipfer[1], N. F. W. Ligterink[1], M. Rubin[1], K. Altwegg[1], N. Hänni[1], D. R. Müller[1], P. Wurz[1], A. Galli[1], and S. F. Wampfler[2]

[1] Space Research & Planetary Sciences, Physics Institute, University of Bern, Sidlerstrasse 5, 3012 Bern, Switzerland
e-mail: kristina.kipfer@unibe.ch, niels.ligterink@unibe.ch
[2] Center for Space and Habitability, University of Bern, Gesellschaftsstrasse 6, 3012 Bern, Switzerland

Received 31 January 2024 / Accepted 22 March 2024

ABSTRACT

Context. Comets are considered to be remnants from the formation of the Solar System. ESA's Rosetta mission targeted comet 67P/Churyumov-Gerasimenko and was able to record high-quality data on its chemical composition and outgassing behaviour, including low abundances of N_2 that are observed to be correlated with H_2O and CO_2 in approximately a 63:37 ratio.
Aims. In this work, the thermal desorption behaviour of N_2 in H_2O:CO_2 ices was studied in the laboratory to investigate the co-desorption behaviour of N_2 within the two most abundant cometary ices in 67P and to derive desorbing fractions in different temperature regimes.
Methods. H_2O:CO_2:N_2 ices of various ratios were prepared in a gas mixing system and co-deposited at 15 K onto a copper sample holder. Sublimation of the ice was measured using temperature programmed desorption mass spectrometry. Quantitative values were derived for the fraction of N_2 co-desorbing with CO_2 and H_2O respectively. To validate the results, H_2O:CO_2:^{13}CO ices were prepared as well.
Results. The experiments show that the co-desorption of N_2 with CO_2 in H_2O:CO_2:N_2 ices depends on the bulk amount of CO_2 present in the ice. The fraction of N_2 trapped in H_2O reduces as more N_2 and CO_2 are added to the mixture. CO behaves qualitatively similar to N_2, but more CO is found to co-desorb with CO_2. To reproduce the ratio of N_2 desorbing with H_2O over that of CO_2 ($N_2(H_2O)/N_2(CO_2)$), our ice analogues need to contain ≥15% CO_2, while 67P contains ≤7.5% CO_2. Large fractions of N_2 can be removed from the ice due to heating up to 70 K, but for ice that most closely resembles that of 67P, the loss fraction of pure phase N_2 is expected to be ≤20%. Therefore, N_2 is suggested to be a minor carrier of nitrogen in the comet.

Key words. astrochemistry – methods: laboratory: molecular – techniques: miscellaneous – comets: individual: 67P/Churyumov-Gerasimenko

1. Introduction

Ices are abundant in the Solar System and beyond (Schmitt et al. 2012; Boogert et al. 2015; Altwegg et al. 2019). This includes cometary nuclei, which consist of dust and ice, and mainly originate from two reservoirs in the Solar System: the Oort Cloud and the Kuiper Belt (Morbidelli et al. 2008). Due to the large distance to the Sun, cometary ices are thought to be mostly pristine and inherited from the solar nebula, thus offering a unique insight into the building blocks of the planets and potentially also into the emergence of molecular complexity on Earth (Drozdovskaya et al. 2019; Altwegg et al. 2019).

Planetary encounters can result in the injection of comets into the inner Solar System (Morbidelli 2005), approaching the Sun. As the surface temperature of the comet increases, molecules sublimate from the near-surface layer and liberated icy grains (A'Hearn et al. 2011). This results in a cometary gas coma, the observation of which allows one to probe the volatile cometary ices. The most abundant molecules in cometary ices are water (H_2O), carbon dioxide (CO_2) and carbon monoxide (CO, Mumma & Charnley 2011; A'Hearn et al. 2012), but observations also revealed a plethora of volatile molecules at minor abundances, such as HCN, H_2S, CH_4, NH_3, C_2H_6, and CH_3OH (e.g., Bockelée-Morvan et al. 2004; Bieler et al. 2015). The various ice components of comets desorb at a wide range of temperatures, starting from sublimation temperatures as low as ~20 K for highly volatile species such as CO and N_2, up to the sublimation temperature of water above 140 K (e.g., Fray & Schmitt 2009; Minissale et al. 2022).

67P/Churyumov-Gerasimenko (henceforth 67P) is a Jupiter-family comet and was the target of the Rosetta mission from 2014 to 2016, which followed this object for two years and investigated its nucleus and coma. Among the scientific objectives of the mission were the investigation of outgassing activity and the composition of cometary volatiles (Glassmeier et al. 2007). The coma of 67P is dominated by water vapour, with CO_2 being the second largest component at 4.5–7.5% (Rubin et al. 2019a; Läuter et al. 2020). Other volatiles, such as CO, H_2S, and O_2 are present at the percent level with respect to water (Hässig et al. 2015; Bieler et al. 2015; Rubin et al. 2019b; Läuter et al. 2020). Patches of high concentration CO_2 ice were observed on 67P's night side, which are the result of gas released from the deeper and warmer interior recondensing on the surface (Filacchione et al. 2016).

The Rosetta mission revealed a rich chemical diversity and complexity in the coma of 67P, more than doubling the number of known cometary molecules (Altwegg et al. 2019), including many volatile species, such as O_2 and CO, up to complex organics (Hänni et al. 2022, 2023). Another important group of molecules are the nitrogen-bearing species. For comets, an overall nitrogen deficiency is observed compared to the solar value, such as investigated for 1P/Halley (Geiss 1988) and C/1995 O1 (Bockelée-Morvan et al. 2000). The nitrogen reservoir is primarily observed in the form of HCN and NH_3 in cometary comae (e.g., Mumma & Charnley 2011; Dello Russo et al. 2016), which are both detected in 67P. Additional, and possible dominant, carriers of nitrogen are ammonium salts and N_2.

N_2 cannot be detected directly in comets with spectroscopic remote sensing techniques, either due to the spectroscopic inactivity of this molecule in the radio and infrared (e.g., Ehrenfreund & van Dishoeck 1998), or due to equipment not being sensitive enough to detect the optical and ultraviolet transitions (e.g., Opitom et al. 2019, 2022). Therefore, only N_2^+ could be detected from ground-based facilities and, for example, revealed comet C/2016 R2 to be nitrogen-rich (Opitom et al. 2019). However, the Rosetta mission marked the first direct detection of N_2 with its ROSINA mass spectrometer suite in a cometary coma (Balsiger et al. 2007), which is present at a bulk abundance of 8.9×10^{-4} with respect to water (Rubin et al. 2019b). While ammonium salts are refractory and expected to reside for a long time in or on 67P, N_2 is a hyper volatile species (sublimation occurs at ~20 K), which means that 67P could have lost significant amounts of N_2 during past heating events.

The abundances of the volatile molecules in 67P have largely been derived from measurements in the cometary coma as the molecules sublimate. The sublimation of highly volatiles, with sublimation temperatures below the one of CO_2, has been shown to correlate with the release of the two major ice components in the comet, H_2O and CO_2 (Rubin et al. 2023). This indicates that likely a trapping mechanism of highly volatile molecules in the less volatile cometary ice phases took place. Rubin et al. (2023) further state, that no pure ice-phase is needed to explain the cometary abundances of such highly volatile molecules, including N_2. These pure ice-phases are suggested to have been lost or to have never been incorporated into the comet.

The trapping of volatiles, including N_2, by water ice has been studied extensively in the laboratory in the past (e.g., Bar-Nun et al. 1985, 1987, 2007, 1998; Notesco & Bar-Nun 1996; Collings et al. 2004; Ninio Greenberg et al. 2017; Laufer et al. 2017). N_2 has been shown to efficiently trap within amorphous water ice, both if it is deposited on the bottom or on top of the water ice (Collings et al. 2004). In the case of trapping, N_2 has been shown to co-desorb with H_2O, once at the phase change of amorphous water to crystalline at ~140 K and when the water itself desorbs at ~160 K. As a consequence, N_2 can be detected well above its free sublimation temperature of ~20 K (Rubin et al. 2023).

CO_2 is a non-negligible component in cometary ices and Simon et al. (2023) have shown that CO_2 can act as an efficient trapping agent of volatiles in its own regard. In their study, they have seen trapping of N_2 by CO_2 ice between 20–60%, depending on the thickness of the ice and CO_2:volatile ratio. However, these studies have predominantly employed binary mixtures of H_2O:volatile and CO_2:volatile, although, as seen in previous trapping experiments, the addition of other molecules can significantly alter the desorption behaviour of a volatile (Collings et al. 2004; Fuchs et al. 2006; Martín-Doménech et al. 2014; Nguyen et al. 2018; Gudipati et al. 2023). To investigate the trapping behaviour of volatiles in a 67P-like cometary ice, ternary mixtures of H_2O:CO_2:volatiles should be studied.

In this study, we investigate the desorption behaviour of the hypervolatile N_2 within H_2O:CO_2 ice and derive quantitative values for the trapping. Furthermore, complementary investigations on the trapping of ^{13}CO are conducted to verify the results, as it is expected to behave in a similar thermodynamic way as N_2. In Sect. 2, the experimental setup and procedures are presented. In Sect. 3, the results of the desorption experiments for various H_2O:CO_2:volatile ice experiments are shown. In Sect. 4 the results are discussed and connected to the observations of comet 67P.

2. Methods

2.1. ICEBEAR

Experiments performed in this study were conducted with the ICEBEAR setup, which is described in detail in Kipfer et al. (2024). A schematic of the setup is shown in the Appendix A. Here, only a brief description of the setup is given: ICEBEAR consists of a stainless steel high vacuum chamber, which reaches base pressures of $<2 \times 10^{-8}$ mbar at room temperature. The pressure is monitored via a pressure gauge (PKR 261, Pfeiffer Vacuum), and a quadrupole mass spectrometer (QMS) is attached to the chamber (QMG 250 M2, Pfeiffer Vacuum). The chamber is pumped using a turbomolecular pump (MAG W 400 iP, Pfeiffer Vacuum), backed by an oilfree roughing pump (SC 15 D, ScrollVac).

In the chamber, a copper sample holder is mounted onto the coldhead of a closed cycle helium cryostat (SRDK Series Cryocooler, Sumitomo Cryogenics). The sample holder is heated via resistive heating using a temperature controller (Lakeshore Model 336).

Gas mixtures are prepared by admixing components in a gas mixing system separate from the main chamber. The pressure in the gas mixing system is monitored using a capacitance diaphragm pressure gauge (CMR 362, Pfeiffer Vacuum) and the gas mixing system is pumped with a turbo pump (HiPace 80, Pfeiffer Vacuum), backed by an oil-free roughing pump (MV 2 NT, Vacuubrand). The gas mixture is introduced into the main vacuum chamber by a manually operated high precision leak valve and deposited onto the sample holder via background gas deposition.

2.2. Measurement procedure

The gas mixtures are prepared in the gas mixing backbone, after it has been thoroughly pumped to remove residual water vapour. First, the hypervolatile species, either N_2 (99.999%, Messer) or ^{13}CO (Cambridge Isotope Laboratories, 99%), are introduced into the gas mixing system, followed by water vapour (MilliQ-grade water, produced with a local Millipore System), and as a last component CO_2 gas (99.995%, Messer). Next, the gases are dosed onto the sample holder, which is cooled to 15 K, with a dosing pressure of 4×10^{-6} mbar for a dosing time of 333 s. We deposit 1000 Langmuir (1.33×10^{-6} mbar s^{-1} = 1 L (Renner et al. 2007)). We assume that 1 L corresponds to one monolayer of material (1 ML = 10^{15} molecules cm^{-2}), therefore the deposited ices are approximated as 1000 ML thick. The gas mixture is deposited via background gas deposition onto the cooled down sample holder. This high pressure deposition method, coupled with the low deposition temperature,

favours the formation of highly porous, amorphous water ice (e.g., Fayolle et al. 2016), which will be discussed in Sect. 4.

Before and during deposition, the pressure in the chamber is logged, while the QMS records the mass over charge (m/z) with a dwell time of 32 ms (N_2 experiments) or 64 ms (^{13}CO experiments) and an electron ionisation energy of 70 eV. An electron current of 2000 µA is used for all experiments and will be discussed in the subsequent section. After gas deposition, the system is left to pump for at least 10 min to remove any gases remaining from the background gas deposition. Afterwards, a temperature programmed desorption (TPD) is started, which is an established technique to study desorption processes of ices and has been applied to the study of cometary ice analogues in previous works (e.g., Burke & Brown 2010; Minissale et al. 2022; Gudipati et al. 2023). During the TPD, the sample holder is heated at a constant heating rate of 2 K min^{-1} from 15 K to at least 250 K. During the warm up phase, the release of volatiles from the sample holder as a function of the temperature is studied by monitoring the signal with the QMS.

Over the course of the TPD experiment, a maximum of 27 ML of water vapour is calculated to have been accumulated from the background in the chamber. The accreted ice most likely differs slightly in morphology from the deposited ice, but based on the temperature is still expected to be amorphous (Fletcher 1971). This, in combination with the low thickness compared to the deposited ice, likely leads to a negligible effect on the trapping.

2.3. Data correction

The QMS measurements in this study have been observed to be subject to an electron current and pressure effect. At low pressure ($\leq 10^{-7}$ mbar), the ratio between electrons emitted by the QMS electron filament and the number of gas particles entering the ionisation region appears to be too large, which results in enhanced fragmentation or double ionisation. In turn, the fragmentation pattern has been observed to vary with pressure, until a high enough pressure ($\geq 10^{-7}$ mbar) is reached, where the pattern remains stable. Unfortunately, the default electron emission current could not be modified at the time of the measurement, and therefore the data are corrected to account for this effect whenever applicable.

All prominent fragment ions of H_2O, CO_2, and N_2 are measured during the experiment. Therefore, the main mass $m/z = 28$ of N_2 overlaps with the fragment of CO_2, which necessitates the tracing of N_2 with the $m/z = 14$ fragment signal.

To correct the signal for the aforementioned pressure effect, every component of the gas mixtures is individually measured at incremental pressure steps, measuring the current with the QMS and creating a calibration curve from both these data, as well as blank measurements, where an H_2O:N_2 ice is measured. For the calibration curve, each fragment is corrected to its stable fragmentation pattern ($F_x(I)$), where I is the total ion current and used as a proxy for the pressure in the system. This correction is applied to all N_2 data presented in this paper and allows for the calculation of the $m/z = 28$ signal from the $m/z = 14$ data. The corresponding figures and correction values are collected in the Appendix B. The correction factor shows with which factor the signal has to be multiplied to reproduce the stable fragmentation pattern. For the ^{13}CO data, a similar data correction was applied, though in this case the m/z = 29 data could be directly corrected due to no overlapping fragmentation pattern with CO_2, as the heavy isotopologue fragments of CO_2 only negligibly contribute to this mass channel. All data presented and used for further analysis have been multiplied with the appropriate factor and have had their baseline subtracted, unless mentioned otherwise.

The abundance of CO_2 and N_2 in the deposited ice with respect to water has been calculated using the formula:

$$R_i = \frac{\phi_{m/z,H_2O}}{\phi_{m/z,i}} \frac{\sigma_{H_2O}}{\sigma_i} \frac{A_i}{A_{H_2O}} \quad (1)$$

where ϕ_i is the respective fragmentation pattern for the molecule for the selected m/z channel, determined from the stable fragmentation pattern observed at high enough pressures, σ_i the total electron impact ionization cross section at 70 eV, and A_i the integrated QMS signal over the course of the TPD. The electron-impact ionization cross sections have been referenced from the NIST database[1] and are $\sigma_{N_2} = 2.508$ Å^2, $\sigma_{CO_2} = 3.521$ Å^2, and $\sigma_{H_2O} = 2.275$ Å^2. For the fragmentation pattern, the following values have been experimentally determined: $\phi_{18,H_2O} = 0.76$, $\phi_{44,CO_2} = 0.79$, and $\phi_{28,N_2} = 0.94$.

3. Results

3.1. TPD traces

Different H_2O:CO_2:N_2 ice mixtures have been prepared to study the desorption behaviour of N_2 from the H_2O:CO_2 ice matrix, using the desorption traces measured with the QMS during the TPD (see Table 1). A selection of these TPDs is shown in Fig. 1. The amount of CO_2 with respect to water increases from left to right, while the amount of N_2 is kept constant. Four distinct desorption events are seen for $m/z = 28$ (N_2): a desorption at ~50 K, a second desorption at ~85 K, a third desorption at ~150 K, and a last, small desorption at ~170 K.

As the amount of CO_2 in the ice increases, another desorption peak emerges for N_2, largely coinciding with the CO_2 desorption peak at 85 K, pointing to trapping of N_2 by CO_2. We refer to a volatile as being trapped by CO_2 (or H_2O) if the volatile co-desorbs with CO_2 (or H_2O). Lastly, both N_2 and CO_2 desorb at ~150 K, which corresponds to the phase change of water from amorphous to crystalline, allowing for previously trapped, more volatile species to desorb. This desorption event is referred to as the 'volcano desorption' (Bar-Nun et al. 1985). A lesser desorption can be seen around ~170 K, which is the H_2O co-desorption. The last two desorption events will be collectively referred to as the combined H_2O release without explicitly distinguishing between them, as these two regimes are unlikely to be distinguishable in the in-situ measurements performed by ROSINA in the coma of comet 67P (Rubin et al. 2023). The desorption events are collected in three desorption regimes, which have been chosen in keeping with the data in Rubin et al. (2023) and are shown in Table 2.

Figure 2 shows the desorption trends of N_2 for selected TPD experiments conducted. The different desorption regimes are indicated as shaded backgrounds. A figure showing all experiments listed in Table 1 can be found in Appendix D. We note here that the selection of different temperature limits for the regimes will result in slightly different values, as the distinction between the CO_2 co-desorption and the combined H_2O release is not trivial, but the behaviour of the data remains consistent. The fraction of N_2 desorbing at the pure N_2 desorption peak (30–60 K) is proportional to the N_2 present in the ice and appears to

[1] https://www.nist.gov/pml/electron-impact-cross-sections-ionization-and-excitation-database

Table 1. Fractions of N_2 desorbing in the various integration regimes for the different ices.

Abundance in the ice [with respect to water]			Molecular concentration [%]			N_2 fraction desorbing		
H_2O	CO_2	N_2	H_2O	CO_2	N_2	Pure N_2 desorption $N_2(N_2$ peak) 30–60 K	Co-Desorption CO_2 $N_2(CO_2)$ 60–115 K	Combined H_2O release $N_2(H_2O)$ 115–200 K
100	0.1	**13.2**	88.3	0.1	11.6	0.418 ± 0.021	0.059 ± 0.012	**0.523 ± 0.033**
100	0.1	5.1	95.1	0.1	4.9	0.339 ± 0.034	0.082 ± 0.016	0.579 ± 0.050
100	2.9	0.7	96.5	2.8	0.7	0.199 ± 0.040	0.100 ± 0.020	0.697 ± 0.060
100	3.2	3.9	93.4	3.0	3.6	0.302 ± 0.030	0.082 ± 0.016	0.617 ± 0.046
100	6.2	3.9	90.8	5.6	3.5	0.326 ± 0.033	0.076 ± 0.008	0.598 ± 0.040
100	7.9	4.7	88.8	7.0	4.1	0.320 ± 0.032	0.091 ± 0.009	0.589 ± 0.041
100	8.4	4.6	88.5	7.5	4.1	0.299 ± 0.060	0.094 ± 0.009	0.607 ± 0.069
100	9.5	0.5	91.0	8.6	0.4	0.156 ± 0.031	0.120 ± 0.012	0.723 ± 0.043
100	11.4	**10.9**	81.8	9.4	8.9	0.490 ± 0.025	0.097 ± 0.010	**0.413 ± 0.034**
100	11.9	0.8	88.7	10.6	0.7	0.206 ± 0.041	0.111 ± 0.006	0.683 ± 0.047
100	13.5	1.2	87.2	11.7	1.1	0.200 ± 0.040	0.135 ± 0.007	0.663 ± 0.047
100	18.0	5.6	81.0	14.5	4.5	0.388 ± 0.039	0.147 ± 0.007	0.463 ± 0.046
100	18.5	6.0	80.4	14.8	4.8	0.370 ± 0.037	0.154 ± 0.008	0.474 ± 0.045
100	20.5	7.0	78.4	16.1	5.5	0.425 ± 0.021	0.159 ± 0.008	0.416 ± 0.029
100	23.1	**11.1**	74.5	17.2	8.3	0.474 ± 0.024	0.165 ± 0.008	**0.360 ± 0.032**
100	24.2	5.3	77.2	18.7	4.1	0.357 ± 0.036	0.173 ± 0.009	0.470 ± 0.044
100	24.8	6.0	76.4	19.0	4.6	0.363 ± 0.036	0.181 ± 0.009	0.456 ± 0.045
100	34.2	1.1	73.9	25.3	0.8	0.228 ± 0.046	0.216 ± 0.011	0.556 ± 0.056

Notes. The desorption regimes are referenced from Table 2 and the temperature limits of the integration have been added for convenience. In the text, the different regimes are referred to by the names given in this table. Please note that small deviations in the desorbing fraction from a total of 1 originate from rounding effects, as well as a small contribution of N_2 in the regions of the integration limits, which were not taken into account. However, this contribution is always less than <0.3% over the whole integration and therefore negligible compared to the error. The data have been sorted with respect to the amount of CO_2 present in the ice. Measurements that use a H_2O:N_2 ratio of ~10:1 are highlighted in bold, including their $N_2(H_2O)$ fraction, and are discussed in Sect. 4.1.

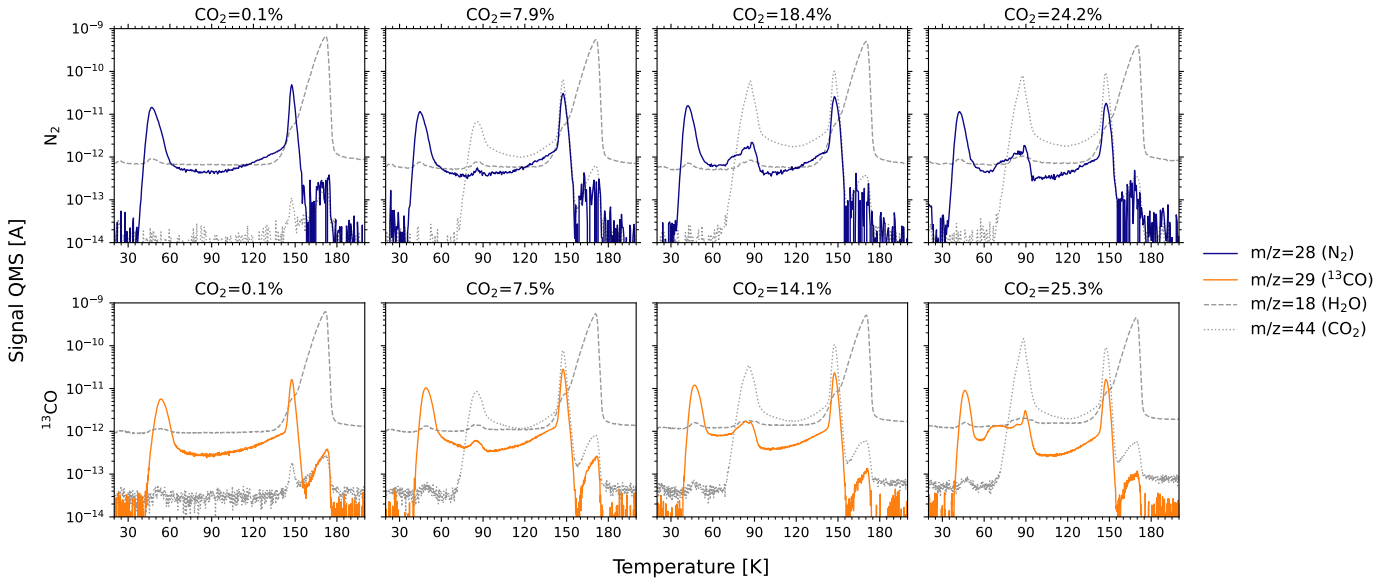

Fig. 1. Desorption traces of N_2 and ^{13}CO in H_2O:CO_2:N_2 and H_2O:CO_2:^{13}CO ices respectively as a function of temperature during the TPD. *Top row*: desorption traces of N_2, (solid, blue), CO_2 (grey, dotted) and H_2O (grey, dashed) for different ice experiments. For the presented data the N_2 contribution has been calculated to be between 3% and 5% with respect to water, therefore assumed to be relatively constant. The CO_2 contribution is shown at the top with respect to water and increases from left to right. For N_2, the corrected data have been calculated from the $m/z = 14$ data, corresponding to the N fragment, as described in Appendix B, therefore resulting in more noise than the ^{13}CO data. Neither the CO_2 nor the H_2O data have been corrected or baseline subtracted for this plot. *Bottom row*: desorption trace for $m/z = 29$ (^{13}CO, orange) for different ice experiments, with the CO_2 and H_2O desorption traces shown as well. The ^{13}CO contributions have been calculated to be between 3% and 4% with respect to water, except for the first experiment, in which the ^{13}CO has been calculated to be ~2.5%. The ^{13}CO signal has been corrected and baseline subtracted, whereas for the CO_2 and H_2O traces no corrections have been performed. Please note that for the ^{13}CO measurements, the background pressure has been higher than for the N_2 measurements, resulting in a larger background for H_2O and CO_2.

Table 2. Different desorption regimes for the volatiles N_2 and CO used for the integration, adapted from Rubin et al. (2023).

Desorption regime	Temperature range [K]	Description
Pure volatile desorption	<60	Highly volatile species are released, such as N_2 and CO.
Co-desorption CO_2	60–115	CO_2 desorption with co-desorption of trapped highly volatiles.
Combined H_2O release	>115	Desorption of trapped highly volatiles and CO_2 during the phase change of H_2O from amorphous to crystalline (volcano desorption Bar-Nun et al. 1985) and the bulk H_2O sublimation.

Notes. Please note the integration limit for the first temperature regime is defined as 10 K lower in this study compared to the cited work.

be only negligibly affected by the amount of CO_2 present. However, a change in the temperature of the desorption onset can be seen, which shifts to higher temperatures as the amount of N_2 in the ice decreases. The shift in desorption temperatures due to interactions between the different ice constituents and trapping is a known effect observed in previous TPD experiments (see e.g., Collings et al. 2004). For all ices, a rapid desorption of N_2 is observed at the volcano desorption, inversely correlated to the amount of N_2 present. Only for small amounts of N_2, a noticeable co-desorption with H_2O can be observed at >150 K.

3.2. N_2 co-desorption with CO_2

For increasing amounts of CO_2 in the H_2O:CO_2:N_2 ices, the prominence and structure of the CO_2 desorption peak at ~85 K increases as well, see Fig. 1, whereas the peak at the volcano desorption remains relatively constant for CO_2 > 5% with respect to water. This indicates that a maximum amount of CO_2 can be trapped within the water, while the remainder desorbs at 85 K. Furthermore, for lower amounts of CO_2, the temperature of the N_2 co-desorption coincides with the CO_2 desorption peak, whereas for ices containing ~15% CO_2, N_2 is observed to co-desorb at the first onset of CO_2 desorption. For CO_2 > 10%, the co-desorption of N_2 with CO_2 can be seen in the normalised desorption trace, see Fig. 2.

Figure 3 shows the signal of N_2 co-desorption with CO_2 (60–115 K) in more detail. The noise in the signal originates from the calculation of the $m/z = 28$ signal from the significantly fainter $m/z = 14$ signal. As the amount of CO_2 increases, the co-desorption trace changes from a single peak to three co-desorption events. For the 100:23.1:11.1 ice, a bump in the desorption is seen before the onset of the CO_2 desorption. This is also observed for two other TPD measurements containing >20% CO_2 and a bit fainter for the ices containing >15% CO_2. The particular shape is likely not an artefact from the data correction, as shown for ^{13}CO in Fig. B.4. The results of Simon et al. (2023) also show such a three-peak structure between 50 and 100 K in both of their CO_2:N_2 (3:1) experiments. Furthermore, the N measured by Gudipati et al. (2023) in their CO:O_2:CO_2:H_2O ice also tentatively shows this particular shape.

This effect is only prominently observed as the amount of CO_2 in the ice increases, therefore the behaviour of the volatile is most likely related to diffusion through the CO_2 ice. In turn, an increased amount of CO_2 in the ice leads to less H_2O in the ice mixture, volatiles could be trapped preferentially by the CO_2 and then desorb as soon as the desorption of CO_2 commences.

3.3. Fraction of desorbing N_2

Figure 4 shows the fraction of N_2 desorbing depending on the desorbing regime. The fractions have been calculated by integrating the desorption trace between the temperature intervals shown in Table 1 and normalising the values to the total N_2 desorption. For the pure N_2 desorption peak ($T < 60$ K), a clear increase in the fraction desorbing as a function of the abundance of N_2 present in the ice can be seen, which was already noted in Fig. 2. For >6% N_2 in the ice, more than 40% of N_2 is expected to be lost during the pure N_2 sublimation peak, whereas for <2%, less than 25% desorbs in the same temperature regime. Notable outliers are the desorption behaviour from the H_2O:N_2 ices, which both yield a lower value than expected from the linear fit.

The data show a clear trend in the desorbing fraction of N_2 as a function of the CO_2 present in the ice mixture, with no apparent dependence on the amount of N_2. It must be noted that for the H_2O:N_2 ices, an integration has been performed as well, though no increased release of N_2 in the temperature region where CO_2 normally desorbs can be seen. Instead, the result corresponds to the observed continuous desorption that occurs after the pure N_2 desorption peak, see Fig. 1.

The trends for the water co-desorption show, that even though the amount of H_2O increases the fraction of N_2 trapped, a clear separation can also be seen depending on the amount of N_2 present in the ice. Therefore, as opposed to the CO_2 co-desorption, not only the amount of H_2O, but also the amount of N_2 in the ice influences the desorption behaviour during the combined H_2O release. However, as CO_2 is also desorbing in this regime, the trapping and desorption of N_2 is more complex, as most likely N_2 is trapped not only within H_2O but also within the H_2O:CO_2 ice matrix.

Figure 5 shows the ratio of N_2 co-desorbing with CO_2 to the sum of CO_2 co-desorption and desorption during the pure N_2 desorption peak. For $CO_2/N_2 < 5$ the fraction of N_2 co-desorbing with CO_2 is observed to increase steeply, whereas for even larger CO_2/N_2 ratios, the slope of the increase reduces significantly. This shows that for all ice mixtures investigated, the pure N_2 desorption peak dominates over the CO_2 co-desorption.

The top row of Fig. 6 shows the ratio of the fraction of N_2 desorbing during the combined H_2O release, labelled as $N_2(H_2O)$, to the fraction of N_2 co-desorbing with CO_2 plus the pure N_2 desorption, labelled as $N_2(CO_2)$+N_2(N_2 peak). The bottom row shows the ratio of $N_2(H_2O)$ to the fraction of N_2 co-desorbing with CO_2, labelled as $N_2(CO_2)$. Indicated as a line is the ratio $N_2(H_2O)/N_2(CO_2)$ of 1.72 derived for 67P (Läuter et al. 2020; Rubin et al. 2023) from the pre-perihelion period of early February 2015 to early September 2016, assuming $CO_2/H_2O = 0.075$. However, a ratio $N_2(H_2O)/N_2(CO_2)$ of 3 is also possible, in the case of $CO_2/H_2O = 0.047$ (Rubin et al. 2019a). The exact ratio depends on if the mission integrated values or the pre-perihelion values are taken. The plots show the ratios once as a function of the N_2 abundance in the ice in the left column and once as a function of the CO_2 in the right column.

For the $N_2(H_2O)/(N_2(CO_2)+N_2(N_2$ peak)) desorption, a slight downward trend can be observed as a function of

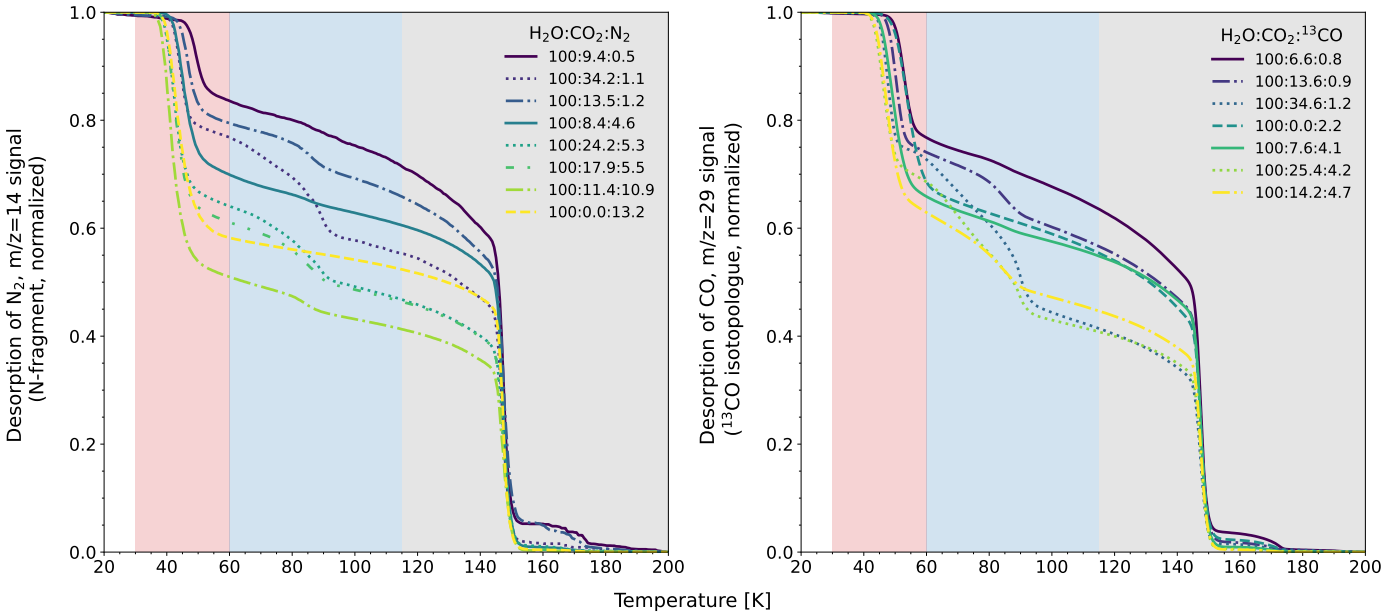

Fig. 2. Normalized desorption behaviour of N_2 and ^{13}CO as a function of temperature in the ices. Please note that not all measured data is displayed. A figure showing the complete data is shown in Appendix D. *Left*: evolution of N_2, calculated from the $m/z = 14$ signal, during the TPD of different ices as a function of the temperature. The data have been sorted with respect to the N_2 present in the ice mixture. The shaded regions correspond to the desorption regions in Table 2. A lighter line color corresponds to more N_2. The linestyles indicate the amount of CO_2 present with respect to water, with the assignment being: $x < 1\%$:dashed, $1 < x < 5\%$: long dashes, $5 < x < 10\%$:solid, $10 < x < 15\%$: dashdot, $15 < x < 20\%$: dashdotdotted, $20 < x\%$: dotted. *Right*: evolution of ^{13}CO, calculated from the $m/z = 29$ signal, as a function of the temperature. The data have been sorted with respect to the ^{13}CO present in the ice mixture. A lighter color corresponds to more ^{13}CO. The linestyles indicate the amount of CO_2 present with respect to water, with the assignment of the linestyles being the same as for the left panel.

increasing N_2 abundance, which is the opposite to the result observed in Fig. 4. Furthermore, for ices with less than 4% N_2, a ratio of <1 can be reached, which indicates that the majority of N_2 is lost before the combined H_2O release. The same plot as a function of CO_2 shows no such clear trend, but instead rather a slight separation depending on the amount of N_2 in the ice.

If only the $N_2(H_2O)/N_2(CO_2)$ ratio is considered, a downward trend is observed as a function of the CO_2 in the ice, with $CO_2 > 15\%$ leading to values in accordance with observations for 67P, and the combined H_2O release is the dominant desorption mechanism. If the same ratio is plotted as a function of N_2, no clear trend in the data is seen.

3.4. Comparison between N_2 and CO desorption

To verify and complement the N_2 data, several measurements have been performed with H_2O:CO_2:CO ices. A list of the ices prepared is shown in Table C.1. CO is more abundant than N_2 in the bulk ice of 67P and is expected to behave in a similar way to N_2 due to their comparable binding energies and desorption temperatures (Minissale et al. 2022; Collings et al. 2004). To distinguish the pure CO signal from the CO fragment originating from the CO_2 fragmentation, isotopically labelled ^{13}CO was used. However, a correction to the signal intensity still had to be applied, see Appendix B.

The bottom row of Fig. 1 shows the TPD traces of various H_2O:CO_2:^{13}CO ice mixtures. Qualitatively, a very similar behaviour to the H_2O:CO_2:N_2 experiments can be seen, with four distinct desorption events. First, a desorption peak corresponding to surface bound ^{13}CO is observed at ~50 K. As the amount of CO_2 increases, the co-desorption peak for ^{13}CO with CO_2 becomes more prominent. Also similar to the H_2O:CO_2:N_2 ices, the co-desorption of ^{13}CO with CO_2 starts before the CO_2 desorption for high CO_2 concentration. Finally, both the volcano desorption and H_2O co-desorption of ^{13}CO are clearly visible. The desorption structure during the CO_2 co-desorption observed for N_2 and described in Sect. 3.2 is observed for ^{13}CO as well for high abundance of CO_2 (>20%). A slight difference in the temperature of the pure desorption peak between N_2 (40–50 K) and ^{13}CO (45–55 K) is noted.

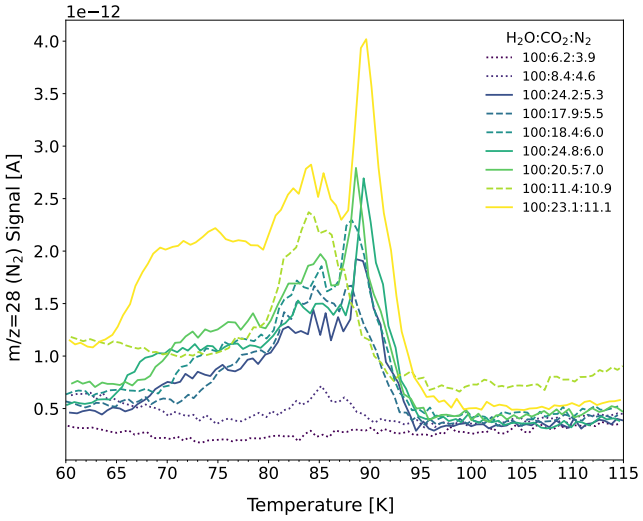

Fig. 3. Zoom in of the N_2 co-desorbing with CO_2. The plots have been color coded for the abundance of N_2 with respect to water. The linestyles indicate the amount of CO_2 present with respect to water, with the assignment being: $x < 10\%$:dotted, $10 < x < 20\%$: dashed, $20 < x\%$: solid. For readability, not all data measured are displayed.

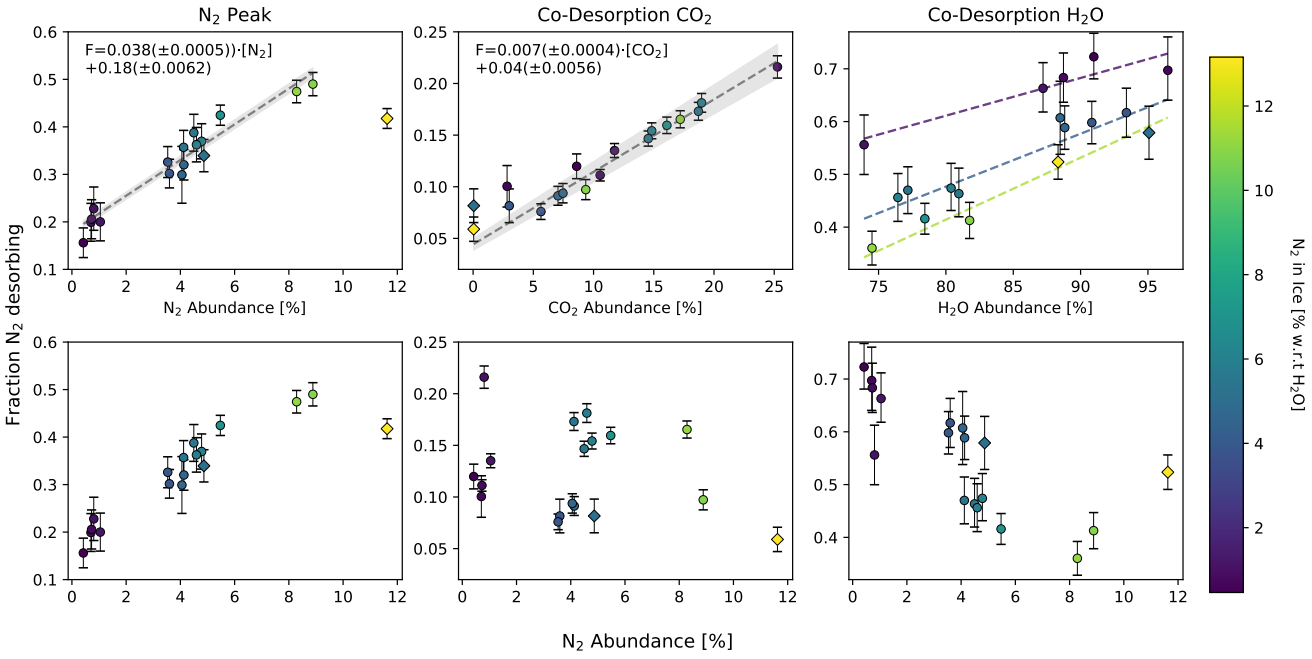

Fig. 4. Desorption behaviour of N_2 in the different regimes, colour coded for the abundance of nitrogen in the ice with respect to water. Each column shows the different desorption events for N_2 with the integration limits for the desorption events given in Table 2. The data points indicated with a diamond are the H_2O:N_2 ices, with negligible amounts of CO_2 in the mixture. The colour assignment is the same as in Fig. 2. *Top row*: desorption behaviour of N_2 as a function of the total N_2 in the mixture, the total CO_2 abundance in the mixture, and the H_2O abundance respectively. The N_2 desorption occurring at the pure N_2 desorption peak and the CO_2 co-desorption have been fitted with a linear function and the resulting best fit is shown in the corresponding panel (grey, dashed line). The grey shaded region indicates the standard deviation of the fit. For the water co-desorption no overall fit has been done, however, trends for the different N_2 abundances have been indicated and colour coded. *Bottom row*: same data as in the top row, but plotted as a function of the total N_2 abundance in the ice mixture.

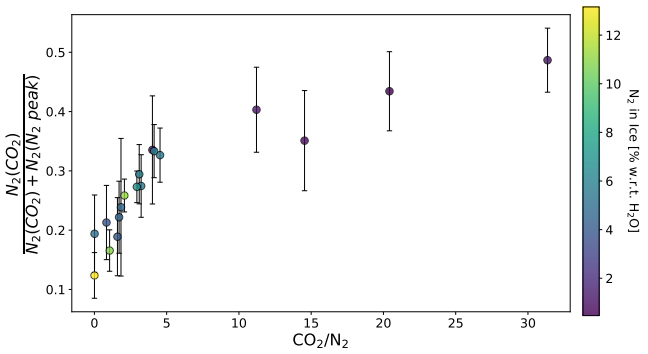

Fig. 5. Fraction of desorbing N_2 during the CO_2 co-desorption compared to the sum of the CO_2 co-desorption and the pure N_2 desorption peak as a function of the CO_2 to N_2 ratio in the ice. The error bars have been calculated using Gaussian error propagation.

In Fig. 7, the fraction of ^{13}CO desorbing for the different temperature regimes is shown. The integration follows the regimes outlined in Table 2. A very similar trend to the H_2O:CO_2:N_2 ices is observed here, with an increase in the desorbing fraction during the pure ^{13}CO desorption as the amount of ^{13}CO increases. Further, the fraction of ^{13}CO co-desorbing with CO_2 also increases as the amount of CO_2 in the ice increases. Again, similar to N_2, the fraction co-desorbing with CO_2 does not appear to depend on the amount of ^{13}CO in the ice but is instead determined by the CO_2 present. However, the linear fit indicates that a larger fraction of the ^{13}CO co-desorbs with CO_2 than N_2 as the amount of CO_2 increases.

4. Discussion and implications

4.1. Desorption experiments

Figure 4 shows that the presence and abundance of both H_2O and CO_2 are important to release volatiles in cometary ices. The fraction of N_2 co-desorbing with CO_2 is a direct function of the CO_2 abundance in the ice. Furthermore, the fraction of N_2 desorbing during the combined H_2O release (that is, volcano and water co-desorption) shows a dependence on the N_2 concentration in the ice, with a higher fraction desorbing for lower concentrations of N_2. This indicates that there is a maximum amount of N_2 that can be trapped in the water ice and for this series of experiments that is approximately 73%, but larger fractions are not ruled out for lower N_2 concentrations. For a higher concentration of N_2 the likelihood that the direct neighbour of an N_2 molecule is neither H_2O nor CO_2, but instead another N_2 increases, resulting in a larger fraction of N_2 desorbing in its pure phase instead of being trapped, in line with recent investigations by Simon et al. (2023).

Ninio Greenberg et al. (2017) investigated H_2O:CO_2:N_2 ices with a thickness of 50–100 µm deposited at ≥30 K and subjected to a heating rate of 1 K min^{-1}. They demonstrated that in the case of CO_2 being present in the ice, volatiles (such as N_2) start to co-desorb with CO_2 as well, instead of only with H_2O. Furthermore, they reported an increase in the trapping efficiency of N_2 in a H_2O:CO_2:N_2 ice compared to a binary H_2O:N_2 ice. However, we note that Ninio Greenberg et al. (2017) determine trapping differently, by comparing the amount of N_2 locked up in the ice after deposition, while we look at fractions of N_2 trapped in – or, associated with – CO_2 and H_2O at 15 K. We conclude that increasing the CO_2 content in the ice, increases N_2 co-release with CO_2, but decreases trapping in the water phase.

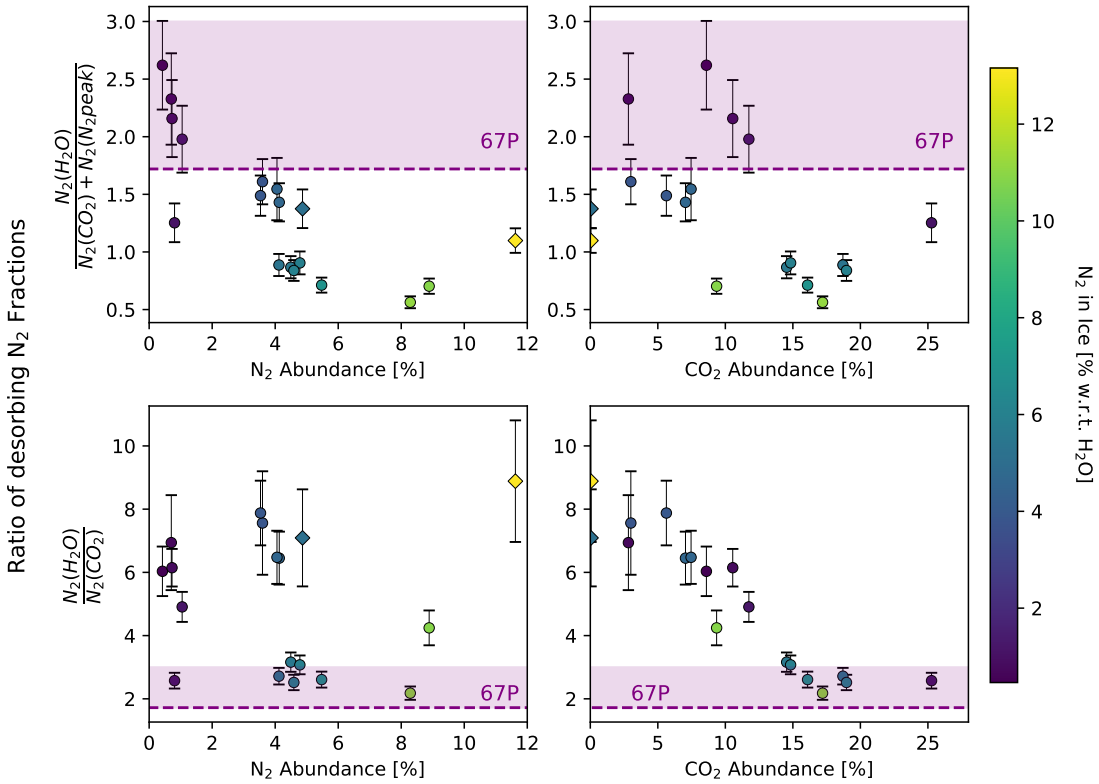

Fig. 6. Ratios of the N_2 fractions desorbing in different desorption regimes. *Top row*: ratio of the N_2 desorption during the combined H_2O release to the sum of the CO_2 and pure N_2 (co-)desorption. The expected ratio of 1.72 for 67P has been indicated (purple, dashed line), as well as the upper limit estimate of 3 (purple, shaded region). *Bottom row*: ratio of the N_2 desorption during the combined H_2O release to the N_2 co-desorption with CO_2. The expected ratio for 67P has been indicated and includes the area between 1.72 (purple, dashed line) and to about 3 (purple, shaded region).

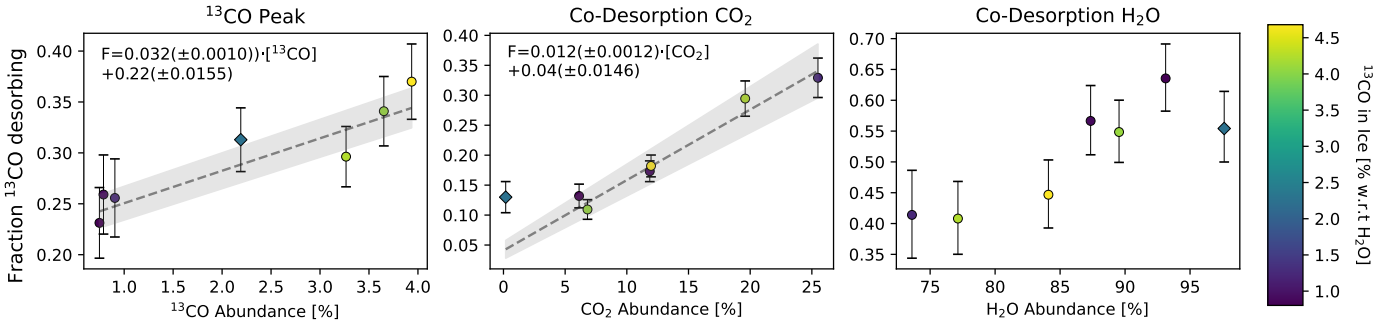

Fig. 7. Desorption behaviour of ^{13}CO in the different regimes, colour coded for the total abundance of ^{13}CO in the ice. Each column shows the different desorption events for ^{13}CO. Diamond markers indicate the experiments without any CO_2. The composition of the ices is collected in Table C.1.

Simon et al. (2023) studied thin film (10 and 50 ML) binary mixtures of H_2O:N_2 and CO_2:N_2, deposited at 12 K, and determined the trapping of N_2 within the two bulk ices. For the mixing ratios of 10:1, they determine that 43 ± 2% of N_2 is trapped in H_2O for the 10 ML case, and 5 8± 2% of N_2 for 50 ML. These values can be compared with our much thicker (1000 ML) ice films, for similar H_2O:N_2 mixing ratios. The relevant experiments are highlighted in bold in Table 1. Our binary H_2O:N_2 experiment shows that the $N_2(H_2O)$ fraction is 52 ± 3%, which is close to the 50 ML values of Simon et al. (2023). We did not investigate ice of thickness between 50 and 1000 ML, but the similarity in trapping fraction suggests that the ice thickness might play a subordinate role in the trapping of N_2 within H_2O for ices with a thickness of ≥50 ML.

However, a comparison with our ternary mixtures, when CO_2 is added, shows that this does affect the $N_2(H_2O)$ trapping efficiency. For an addition of ∼11% CO_2 (w.r.t. H_2O), $N_2(H_2O)$ decreases to 41 ± 3%, while for ∼23% added CO_2 $N_2(H_2O)$ is reduced further to 36 ± 3%. This effect is likely caused by competition for binding sites between different molecular constituents. These experimental observations stress the importance of using realistic ice compositions when investigating cometary or interstellar ice analogues due to the influence the different components have on the overall behaviour of the

ice. Nevertheless, binary mixtures are valuable when investigating chemical extremes.

We observe N_2 and CO to behave qualitatively similar during the TPDs. However, a comparison between Figs. 4 and 7 shows that a larger portion of CO co-desorbs with CO_2 as compared to the ices containing N_2 (see the results in Tables 1 and C.1). The results from Simon et al. (2023) show similar entrapment efficiencies for N_2 and CO for the 10:1 50 ML experiments in both the CO_2 and H_2O ices, whereas the results in our study indicate more efficient trapping in CO_2 for CO in the H_2O:CO_2 matrix than for N_2. The fractions of CO and N_2 trapped in H_2O are comparable. Bar-Nun et al. (2007) have linked differences in the N_2 and CO desorption behaviour in amorphous water ice to the dipole moment (or lack thereof) of the volatile gases, which is expected to influence their trapping efficiencies in the pores of the amorphous ice. It is possible that a similar effect is taking place with regard to the H_2O:CO_2 ice, as the N_2 molecule does not have a dipole moment.

In Gudipati et al. (2023) a CO:O_2:CO_2:H_2O (1:1:2:6) ice with residual N_2 was thermally desorbed. The results show a different behaviour of CO and N_2 release, with 70% of CO desorbing during the pure volatile desorption at <70 K, whereas 38.8% of N_2 desorb in the same temperature range. However, care must be taken with the N_2 results from their work, as N_2 is only a residual component in the gas mixture and was not a controlled contribution in the initial mixture. Nevertheless, extrapolating from the N_2 data to CO and vice versa is not trivial and care should be taken when using one as a proxy for the other to derive quantitative values, even though their qualitative behaviour in the H_2O:CO_2 matrix is similar. Furthermore, future experiments should also consider the four-component ice mixture H_2O:CO_2:CO:N_2, as the qualitatively similar behaviour of N_2 and CO in both the binary H_2O and CO_2 ices, as well as the H_2O:CO_2 ice suggests that they might be competing for the same binding sites (Simon et al. 2023). Such an effect was observed by Ninio Greenberg et al. (2017) for N_2 and argon, where the two volatiles appear to interfere with each other when deposited together, leading to lower trapping efficiencies by H_2O. A similar effect might explain the differing desorption behaviour of CO and N_2 in Gudipati et al. (2023).

4.2. Implications for comet 67P

As 67P is thought to have inherited most of its volatile material from ice-coated grains in the prestellar cloud that the Solar System formed from (e.g., Altwegg et al. 2017; Drozdovskaya et al. 2019), the present and historic N_2 content has astrochemical implications.

The N_2 abundances in this study have been chosen high compared to the bulk abundance of N_2 in 67P, which is expected to be in the range of 8.9×10^{-4} with respect to water (Rubin et al. 2019a). A realistic CO_2/N_2 ratio of 52.8–85.7 for 67P (Rubin et al. 2019a,b) can be expected, which is higher than the ratios investigated in this study (maximum of ~33, see Fig. 5). The maximum fraction of N_2 co-desorbing with CO_2 in this measurement series has been observed to be ~20%. However, as addressed in Sect. 3.1, this value might be overestimated due to the continuous desorption of N_2 after the N_2 peak, therefore the 20% should rather be considered an upper limit.

The temperatures in the outgassing layers of 67P are poorly constrained. Its brightness temperature has been measured to be in the range of 60–180 K (Gulkis et al. 2015) at an orbital distance of 3.2 au and further increases as the comet approaches perihelion. Nevertheless, there might be regions on 67P where the temperature required for the phase transition of water is never reached, resulting in a slow sublimation of the water ice and the trapped volatile species within (Rubin et al. 2023). Thermal heating of up to 0.1 K min^{-1} (Gulkis et al. 2015), or locally between 2 and 9 K min^{-1} (Tosi et al. 2019) could be possible on the surface. However, as the field of view is large for ROSINA, the gas could originate from various parts of the surface, in particular the illuminated areas with direct line-of-sight.

Rubin et al. (2023) investigated the desorption behaviour of volatiles in 67P and found that the N_2 release correlates with CO_2 and H_2O outgassing. No unassociated, pure phase N_2 is observed. For a $CO_2/H_2O = 0.047$ bulk ratio of 67P (Rubin et al. 2019a), 25% of N_2 was found to be associated with CO_2 and 75% with H_2O, while for a $CO_2/H_2O = 0.075$ ratio (Läuter et al. 2020) 37% N_2 were found to be associated with CO_2 and 63% with H_2O. Similarly to N_2, the CO release in 67P was also observed to correlate with CO_2 and H_2O (Rubin et al. 2023): For a $CO_2/H_2O = 0.047$ ratio, 20% of CO was found to be associated with CO_2 and 80% with H_2O, while for a $CO_2/H_2O = 0.075$ ratio, 30% CO were associated with CO_2 and 70% with H_2O.

N_2 and CO show qualitatively similar behaviour in the observations of 67P, as well as in the analogue ice experiments. However, between 67P observations and experiments, discrepancies become apparent. The bulk behaviour of 67P results in $N_2(H_2O)/N_2(CO_2)$ ratios of 3 and 1.7, depending on the value chosen for its CO_2 bulk abundance. In our study, a bulk molecular fraction of ≥15% CO_2 is needed in the ice to yield this $N_2(H_2O)/N_2(CO_2)$ ratio (Fig. 6). A number of explanations are suggested for this discrepancy. First, measurement errors are large for ROSINA measurements of N_2, because its mass (m/z = 28.0056) is close to that of CO (m/z = 27.9944), resulting in mass spectrometric interference and larger uncertainties on abundances and correlations. Second, Rubin et al. (2023) showed that there are times in the mission where the CO_2 signal dominates over the H_2O signal. This could indicate sublimation from regions where the temperature of the sublimating layer is high enough for CO_2, but not H_2O, enhancing therefore CO_2/H_2O ratio. In fact, Läuter et al. (2018) showed that the surface emission regions of CO_2 on 67P remained nearly constant over the mission, whereas H_2O emission regions followed the subsolar latitude, pointing to differences in the CO_2/H_2O emission over the course of the mission likely being related to the temperature of the sublimating layers. However, the gas phase measurements might not be representative of the bulk ice composition in the interior of the comet. Third, we have seen before that an increase in CO_2 content reduces the $N_2(H_2O)$ fraction, presumably due to competition for binding sites. Other molecules likely have a similar effect on the ice. While CO_2 is the second most abundant species in the cometary ice of 67P and therefore has the largest impact, the combined effect of multiple minor species could have a similarly large effect on the competition for binding sites and reduce the trapping of N_2 in H_2O.

An ongoing and still unresolved question is the morphology of 67Ps ice (e.g., Marboeuf et al. 2012, and references therein). Thomas et al. (2019) summarized the open questions after the Rosetta mission, such as whether the water ice in 67P is in amorphous or crystalline form. Constraints on this question could give information about the formation conditions of 67P, such as if it formed by agglomerating pristine water ice grains from the insterstellar medium (Owen & Bar-Nun 1993), or possibly from grains containing clathrates (Mousis et al. 2000).

The measurement protocol chosen for our experimental campaign favours the formation of highly porous, amorphous ice, which is expected to efficiently trap volatiles (Ayotte et al.

2001) and could be present on 67P if it formed in or inherited its icy material from a cold reservoir, such as a dark cloud. For comet Halley, crystallization of amorphous water ice in the nucleus was theorized to be responsible for an observed outburst (Prialnik & Bar-Nun 1992), though Kouchi & Sirono (2001) have shown that impurities in the amorphous water ice could lead to the transition being endothermic.

Future missions targeting comets, especially missions involving a possible cryogenic sample return of ice, such as the AMBITION mission concept (Bockelée-Morvan et al. 2022), could give valuable insight into the morphology of the ice and guide future laboratory experiments for cometary ice analogues.

4.3. The 'missing' nitrogen problem

Rubin et al. (2019a) shows the elemental nitrogen abundance relative to silicon for 67P, which is depleted by about one order of magnitude compared to the solar value for assumed dust-to-ice ratios of 3 and 1 (see their Fig. 5). Similarly, Geiss (1988) suggested a nitrogen depletion in comet 1P/Halley.

Observations of the ice inventories of interstellar clouds have shown that the nitrogen-bearing molecules only account for a fraction of the elemental nitrogen budget (e.g., ∼11% for sources observed with *Spitzer*, Öberg et al. 2011). The solution to this interstellar 'missing' nitrogen problem has been suggested to be found in N_2 (Palumbo et al. 2000), which is only weakly spectroscopically active in the infrared wavelength regime that interstellar ices are observed in. This has resulted in the suggestion that the majority of the elemental nitrogen budget is locked up in N_2 on ice-coated interstellar dust grains. This hypothesis has been used to explain Jupiter's super-solar nitrogen abundance, with a scenario where this planet formed outside the N_2 snow line (located at ∼30 au in the protosolar nebula), where N_2 on ice grains accounted for 90% of the elemental nitrogen budget (Öberg & Wordsworth 2019; Bosman et al. 2019). However, searches for N_2 in interstellar ice have resulted in a large range of upper limit abundances (≤0.2–60% w.r.t. H_2O, Elsila et al. 1997; Sandford et al. 2001; Boogert et al. 2002, 2015), but no secure detection to date. Currently, the ROSINA detection of N_2 in comet 67P provides the only indication of the N_2 content in interstellar ice.

The discussion in Sects. 4.1 and 4.2 suggests that 67P, or the ice it is made of originally, could have contained more N_2 than observed at the present. During the Centaur-phase of 67P, if the internal temperature increased up to 70 K (Guilbert-Lepoutre et al. 2016), N_2 in its pure phase could have been lost. However, the results from Fig. 4 show that the fraction of N_2 desorbing during the pure N_2 desorption depends on the amount of N_2 present in the ice. In other words, the lower the N_2 concentration, the smaller the fraction of N_2 released in its pure form. Since the current N_2 content in 67P (∼0.09% w.r.t. H_2O) is lower than the fractions used in this study, this indicates that the fraction lost for 67P is low and probably ≤20%. Furthermore, as shown in Notesco & Bar-Nun (2005), thicker ices (>5 µm) are more likely to trap impurities such as N_2 and other volatiles. Therefore, for cometary ices, their thickness would suggest that the majority of N_2 remained trapped.

A neglected aspect in this regard is the timescale. As even the most realistic laboratory experiments cannot reproduce cometary timescales, desorption of trapped N_2 might have occurred slowly due to diffusion through the bulk ice, resulting in a steady desorption of N_2, in particular upon moderate heating up to 70 K. While this could mean that more N_2 was historically present in the ice of 67P, such a scenario would not fit with CO. Carbon monoxide has a similar desorption temperature (desorption parameters) and shows qualitatively similar desorption behaviour to N_2. This indicates that both species might have been similarly affected and depleted during the history of 67P. Since 67P at present contains more CO (3.1%) than N_2 (0.09%), historic abundances quickly run into limitations. For example, if 67P or the material it formed from started with 1% N_2, then, assuming a constant ratio between the species, ∼30% CO was present. While such CO ice abundances are still realistic for comets and interstellar ices (Mumma & Charnley 2011; Boogert et al. 2015), larger factors of increase become increasingly less realistic. Therefore, it is a possibility that N_2 was never a major component in 67P or the material it formed from and its loss is not sufficient to account for the missing nitrogen in this comet.

Another explanation for the missing nitrogen is suggested to be the presence of ammonium salts in 67P (Altwegg et al. 2020, 2022). Evidence for such salts in the comet has been detected during a dust impact, where fragments associated with ammonium salts were measured over several hours (Altwegg et al. 2020). Furthermore, VIRTIS-M measurements of 67P show a good agreement between the observed spectrum of the surface and laboratory reference measurements of ammonium salts (Poch et al. 2020).

As the results obtained in the present study suggest that the loss of N_2 in 67P might not be sufficient to explain the nitrogen deficiency, this could in turn support the hypothesis of nitrogen being found in the form of ammonium salts. This would allow for the nitrogen to survive at higher temperatures than the sublimation of water ice (Altwegg et al. 2022), but also partly evade detection in the gas phase due to the high sublimation temperature.

More research and observations are required to determine the role ammonium salts can play in the search for the missing nitrogen. For such an endeavour, more sensitive instruments are needed, such as the JWST, which could potentially make a direct, remote detection of such salts possible (Altwegg et al. 2022).

5. Conclusions and outlook

We presented TPD measurements three-component ice mixtures consisting of H_2O:CO_2:N_2 and H_2O:CO_2:CO. We investigated the desorption behaviour of the volatiles (N_2 and CO) as a function of the temperature and ice composition, and contextualised the results within the framework of comet 67P results. Systematic studies of such ternary mixtures containing H_2O and CO_2 have been neglected by laboratory work to this date. Our findings and outlook are summarised below:

1. Our experiments with H_2O:CO_2:N_2 ices showed that 15.6–49.0% of N_2 desorbs during the pure N_2 desorption and that this fraction increases the larger the N_2 content in the mixture is. 7.6–21.6% of N_2 co-desorbs with CO_2 and this amount increases with increasing CO_2 content in the ice. Finally, between 36.0–72.3% of N_2 desorbs during the combined H_2O release (that is, volcano desorption and water co-desorption combined), where lower N_2 quantities in the ice result in larger fractions released with H_2O. The behaviour of H_2O:CO_2:CO ice is qualitatively largely identical to its N_2 counterpart, but a larger fraction of CO is observed to co-desorb with CO_2.
2. A comparison between binary and ternary H_2O-dominated mixtures shows that more complex ice mixtures affect the trapping efficiency of N_2 in H_2O, which is explained by

an increased competition for binding sites when more components are present in the mixture. To assess the trapping behaviour of cometary or interstellar ice, realistic ice mixtures need to be used.

3. The measured $N_2(H_2O)/N_2(CO_2)$ ratio (that is, N_2 trapped in water over N_2 embedded in CO_2) in 67P is in the range of 1.7–3.0. To match such values, the H_2O:CO_2:N_2 ice used in our experiments must contain >15% CO_2, while the CO_2 bulk value of 67P is likely ≤7.5% (Läuter et al. 2020). For realistic CO_2 bulk abundances in 67P, a ratio of $N_2(H_2O)/N_2(CO_2)$ between 6 to 9 would be expected based on the present experiments. Local variations in ice composition and temperature of the sublimating layers of 67P are thought to significantly influence the observed gas ratios in the coma during the Rosetta mission.
4. For realistic bulk N_2 abundances in 67P, a maximum of 20% of N_2 is expected to desorb before 70 K. Consequently, relatively little N_2 has been lost from 67P if it underwent a heating event (that is, Centaur stage). Therefore, loss of N_2 likely cannot account for the approximately one order of magnitude elemental nitrogen deficiency of comet 67P compared to the solar elemental composition. Assuming 67P inherited most of its ice from a prestellar environment, the amount of elemental nitrogen locked up in N_2 on the ice-coated dust grains forming 67P is suggested to be at most a few percent with respect to H_2O.

As a Jupiter-family comet, 67P might have undergone substantial heating in the past before and while it moved to its current orbit. Data from the Comet Interceptor mission (Jones et al. 2024), which will potentially target a pristine and dynamically new comet, can help understand mechanisms that alter the surface and bulk ice composition of comets. Its MANiaC mass spectrometer will be instrumental in detecting highly volatile species. Additional laboratory measurements on more complex and realistic ice mixtures will be necessary to interpret this data.

Acknowledgements. The authors want to thank the Reviewer, Marco Minissale, for his insightful comments which have helped improve the quality of the paper. K.A.K. and N.F.W.L. acknowledge support from the Swiss National Science Foundation (SNSF) Ambizione grant 193453 and NCCR PlanetS. Work by M.R., N.H., and D.R.M. was funded by the Canton of Bern and the Swiss National Science Foundation (SNSF; 200020_207312). S.F.W acknowledges the financial support of the SNSF Eccellenza Professorial Fellowship (PCEFP2_181150).

References

A'Hearn, M. F., Belton, M. J. S., Delamere, W. A., et al. 2011, Science, 332, 1396
A'Hearn, M. F., Feaga, L. M., Keller, H. U., et al. 2012, ApJ, 758, 29
Altwegg, K., Balsiger, H., Berthelier, J. J., et al. 2017, Phil. Trans. Royal Soc. A: Math. Phys. Eng. Sci., 375, 20160253
Altwegg, K., Balsiger, H., & Fuselier, S. A. 2019, ARA&A, 57, 113
Altwegg, K., Balsiger, H., Hänni, N., et al. 2020, Nat. Astron., 4, 533
Altwegg, K., Combi, M., Fuselier, S., et al. 2022, MNRAS, 516, 3900
Ayotte, P., Smith, R. S., Stevenson, K. P., et al. 2001, J. Geophys. Res., 106, 33387
Balsiger, H., Altwegg, K., Bochsler, P., et al. 2007, Space Sci. Rev., 128, 745
Bar-Nun, A., & Owen, T. 1998, in Trapping of Gases in Water Ice and Consequences to Comets and the Atmospheres of the Inner Planets, eds. B. Schmitt, C. De Bergh, & M. Festou (Dordrecht: Springer), 353
Bar-Nun, A., Herman, G., Laufer, D., & Rappaport, M. 1985, Icarus, 63, 317
Bar-Nun, A., Dror, J., Kochavi, E., & Laufer, D. 1987, Phys. Rev. B, 35, 2427
Bar-Nun, A., Notesco, G., & Owen, T. 2007, Icarus, 190, 655
Bieler, A., Altwegg, K., Balsiger, H., et al. 2015, Nature, 526, 678
Bockelée-Morvan, D., Lis, D. C., Wink, J. E., et al. 2000, A&A, 353, 1101
Bockelée-Morvan, D., Crovisier, J., Mumma, M. J., & Weaver, H. 2004, in Comets II, eds. M. C. Festou, H. A. Weaver, & H. U. Keller (Tucson: Univ. of Arizona), 391
Bockelée-Morvan, D., Filacchione, G., Altwegg, K., et al. 2022, Exp. Astron., 54, 1077
Boogert, A. C. A., Hogerheijde, M. R., Ceccarelli, C., et al. 2002, ApJ, 570, 708
Boogert, A. C. A., Gerakines, P. A., & Whittet, D. C. B. 2015, ARA&A, 53, 541
Bosman, A. D., Cridland, A. J., & Miguel, Y. 2019, A&A, 632, L11
Burke, D. J., & Brown, W. A. 2010, Phys. Chem. Chem. Phys., 12, 5947
Collings, M. P., Anderson, M. A., Chen, R., et al. 2004, MNRAS, 354, 1133
Dello Russo, N., Kawakita, H., Vervack, R. J., & Weaver, H. A. 2016, Icarus, 278, 301
Drozdovskaya, M. N., van Dishoeck, E. F., Rubin, M., Jørgensen, J. K., & Altwegg, K. 2019, MNRAS, 490, 50
Ehrenfreund, P., & van Dishoeck, E. 1998, AdSpR, 21, 15
Elsila, J., Allamandola, L. J., & Sandford, S. A. 1997, ApJ, 479, 818
Fayolle, E. C., Balfe, J., Loomis, R., et al. 2016, ApJ, 816, L28
Filacchione, G., Raponi, A., Capaccioni, F., et al. 2016, Science, 354, 1563
Fletcher, N. H. 1971, Rep. Progr. Phys., 34, 913
Fray, N., & Schmitt, B. 2009, Planet. Space Sci., 57, 2053
Fuchs, G. W., Acharyya, K., Bisschop, S. E., et al. 2006, Faraday Discuss., 133, 331
Geiss, J. 1988, Cosmic Chemistry (New York: Springer), 1
Glassmeier, K.-H., Boehnhardt, H., Koschny, D., Kührt, E., & Richter, I. 2007, Space. Sci. Rev., 128, 1
Gudipati, M. S., Fleury, B., Wagner, R., et al. 2023, Faraday Discuss., 245, 467
Guilbert-Lepoutre, A., Rosenberg, E. D., Prialnik, D., & Besse, S. 2016, MNRAS, 462, S146
Gulkis, S., Allen, M., von Allmen, P., et al. 2015, Science, 347, aaa0709
Hänni, N., Altwegg, K., Combi, M., et al. 2022, Nat. Commun., 13, 3639
Hänni, N., Altwegg, K., Baklouti, D., et al. 2023, A&A, 678, A22
Hässig, M., Altwegg, K., Balsiger, H., et al. 2015, Science, 347, aaa0276
Jones, G. H., Snodgrass, C., Tubiana, C., et al. 2024, Space Sci. Rev., 220, 9
Kipfer, K. A., Galli, A., Riedo, A., et al. 2024, Icarus, 410, 115742
Kouchi, A., & Sirono, S.-I. 2001, Geophys. Res. Lett., 28, 827
Laufer, D., Bar-Nun, A., & Ninio Greenberg, A. 2017, MNRAS, 469, S818
Läuter, M., Kramer, T., Rubin, M., & Altwegg, K. 2018, MNRAS, 483, 852
Läuter, M., Kramer, T., Rubin, M., & Altwegg, K. 2020, MNRAS, 498, 3995
Marboeuf, U., Schmitt, B., Petit, J. M., Mousis, O., & Fray, N. 2012, A&A, 542, A82
Martín-Doménech, R., Caro, G., Bueno, J., & Goesmann, F. 2014, A&A, 564
Minissale, M., Aikawa, Y., Bergin, E., et al. 2022, ACS Earth Space Chem., 6, 597
Morbidelli, A. 2005, arXiv e-prints [arXiv:astro-ph/0512256]
Morbidelli, A., Levison, H. F., & Gomes, R. 2008, The Solar System beyond Neptune (Tucson: University of Arizona Press), 275
Mousis, O., Gautier, D., Bockelée-Morvan, D., et al. 2000, Icarus, 148, 513
Mumma, M. J., & Charnley, S. B. 2011, ARA&A, 49, 471
Nguyen, T., Baouche, S., Congiu, E., et al. 2018, A&A, 619, A111
Ninio Greenberg, A., Laufer, D., & Bar-Nun, A. 2017, MNRAS, 469, S517
Notesco, G., & Bar-Nun, A. 1996, Icarus, 122, 118
Notesco, G., & Bar-Nun, A. 2005, Icarus, 175, 546
Öberg, K. I., & Wordsworth, R. 2019, AJ, 158, 194
Öberg, K. I., Boogert, A. C. A., Pontoppidan, K. M., et al. 2011, ApJ, 740, 109
Opitom, C., Hutsemékers, D., Jehin, E., et al. 2019, A&A, 624,
Opitom, C., Snodgrass, C., Forgia, F., et al. 2022, Exp. Astron., 55, 1
Owen, T., & Bar-Nun, A. 1993, Nature, 361, 693
Palumbo, M., Strazzulla, G., Pendleton, Y., & Tielens, A. 2000, ApJ, 534, 801
Poch, O., Istiqomah, I., Quirico, E., et al. 2020, Science, 367, eaaw7462
Prialnik, D., & Bar-Nun, A. 1992, A&A, 258, L9
Renner, T., Cohen, E. R., Cvitas, T., et al. 2007, Quantities,Units and Symbols in Physical Chemistry (The Royal Society of Chemistry), 248
Rubin, M., Altwegg, K., Balsiger, H., et al. 2019a, MNRAS, 489, 594
Rubin, M., Bekaert, D. V., Broadley, M. W., Drozdovskaya, M. N., & Wampfler, S. F. 2019b, ACS Earth Space Chem., 3, 1792
Rubin, M., Altwegg, K., Berthelier, J.-J., et al. 2023, MNRAS, 526, 4209
Sandford, S. A., Bernstein, M. P., Allamandola, L. J., Goorvitch, D., & Teixeira, T. V. S. 2001, ApJ, 548, 836
Schmitt, B., de Bergh, C., & Festou, M. 2012, Solar System Ices: Based on Reviews Presented at the International Symposium "Solar System Ices" held in Toulouse, France, on March 27–30, 1995 (Netherlands: Springer), Astrophys. Space Sci. Lib.
Simon, A., Rajappan, M., & Öberg, K. I. 2023, ApJ, 955, 5
Thomas, N., Ulamec, S., Kührt, E., et al. 2019, Space Sci. Rev., 215
Tosi, F., Capaccioni, F., Capria, M. T., et al. 2019, Nat. Astron., 3, 649

Appendix A: Chamber

The schematic of the chamber is shown in Fig. A.1.

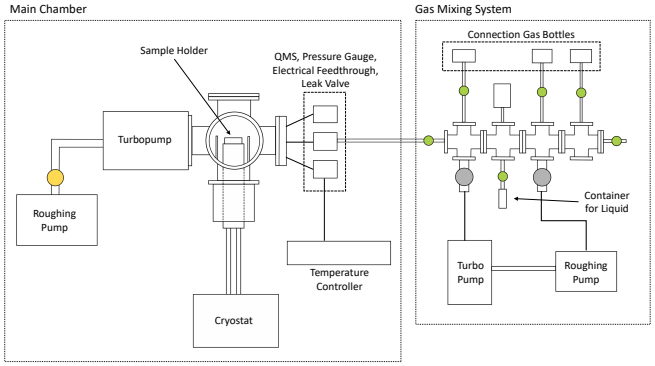

Fig. A.1. Schematic Drawing of the ICEBEAR setup, highlighting the two parts: the main chamber and the separate gas mixing system. The figure was reproduced and adapted from Kipfer et al. (2024).

Appendix B: Correction factor

Both the function and the fitting values for the fractionation curve for N_2, CO_2 and ^{13}CO are shown in Table B.1. For H_2O there was no necessity to perform a correction due to a high enough pressure during its desorption. Figure B.1 shows the correction for m/z=14 and m/z=28 and the subsequently fitted factor, with which the data are then multiplied to reproduce the data. Figure B.2 shows the correction factor derived for m/z=44 for CO_2, Fig. B.3 the correction for ^{13}CO. Figure B.4 shows the direct comparison between raw measured data for ^{13}CO versus the corrected data for the CO_2 co-desorption regime. Figure B.5 shows the N_2 and CO_2 correction applied to all data used for this work. The corrected data are then further analysed and integrated.

Table B.1. Values for the fit of the fractionation.

Molecule	Function	a	b	c
N_2 (m/z=14)	$a\cdot e^{(-b\cdot x)}+c$	0.466	4.724	0.062
N_2 (m/z=28)	$a\cdot e^{(-b\cdot x)}+c$	-0.467	4.372	0.930
CO_2 (m/z=44)	$a\cdot e^{(-b\cdot x)}+c$	-0.481	1.866	0.771
^{13}CO (m/z=29)	$a\cdot e^{(-b/x)}+c$	0.473	0.052	0.503

Notes. This value is then used to further determine the correction factor, which is the value with which the data are multiplied to reproduce the fragmentation pattern. Please note that to fit the data, the total signal had to be multiplied by a factor of 10^{10}. For the ^{13}CO data, a different formula has been used, which gave better results.

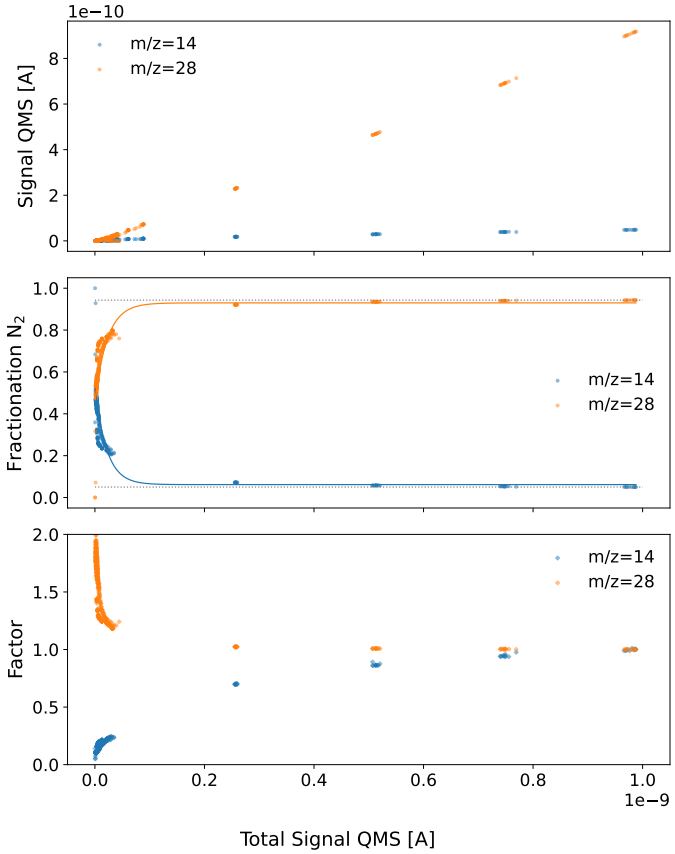

Fig. B.1. Investigation of the fractionation of m/z=28 and m/z=14 as a function of the Total Signal measured with the QMS from three different calibration measurements. This highlights the need for a correction of the data. The top panel shows the evolution of the signal measured with the QMS for both mass channels. The middle panel shows the fractionation pattern. The constant value reached at high enough Signal has been marked with a grey dotted line. The bottom panel then shows the factor with which the data have to be multiplied as a function of the total signal to obtain the 'true fragmentation', which is shown in the middle panel as the dotted line. The details of the fit shown in the middle panel are collected in Table B.1.

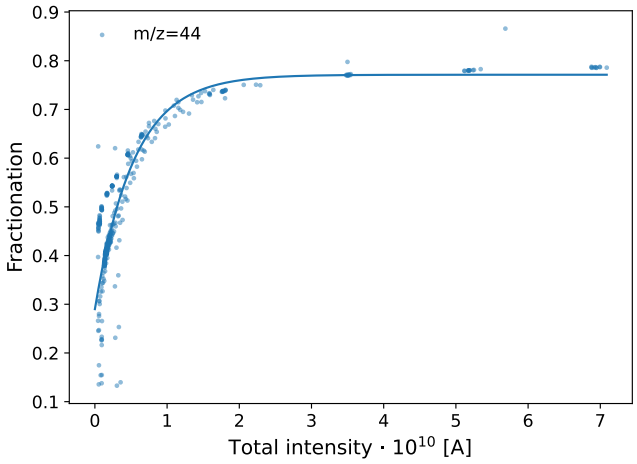

Fig. B.2. Fractionation of m/z=44 as a function of the total intensity measured with the QMS for the relevant CO_2 mass channel. Three different calibration measurements were used.

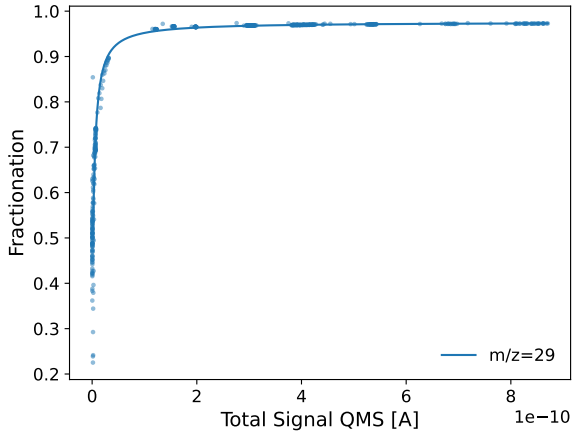

Fig. B.3. Fractionation of m/z=29 as a function of the total intensity measured with the QMS for the relevant ^{13}CO mass channel. Two different calibration measurements were used.

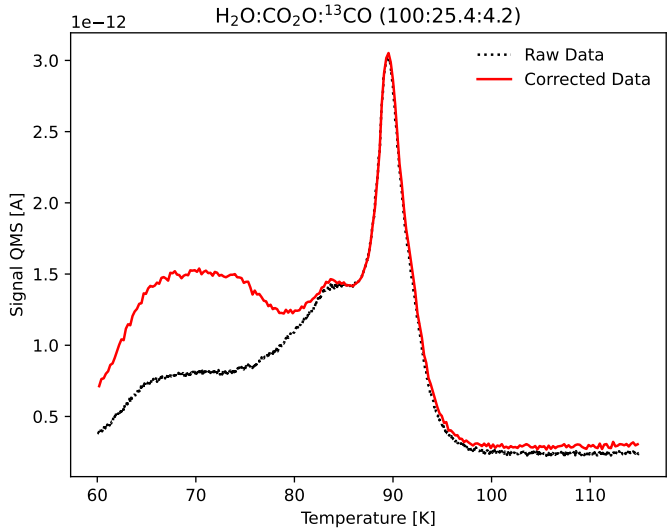

Fig. B.4. Comparison between the raw data measured with the QMS and the corrected data for a H_2O:CO_2:^{13}CO ice.

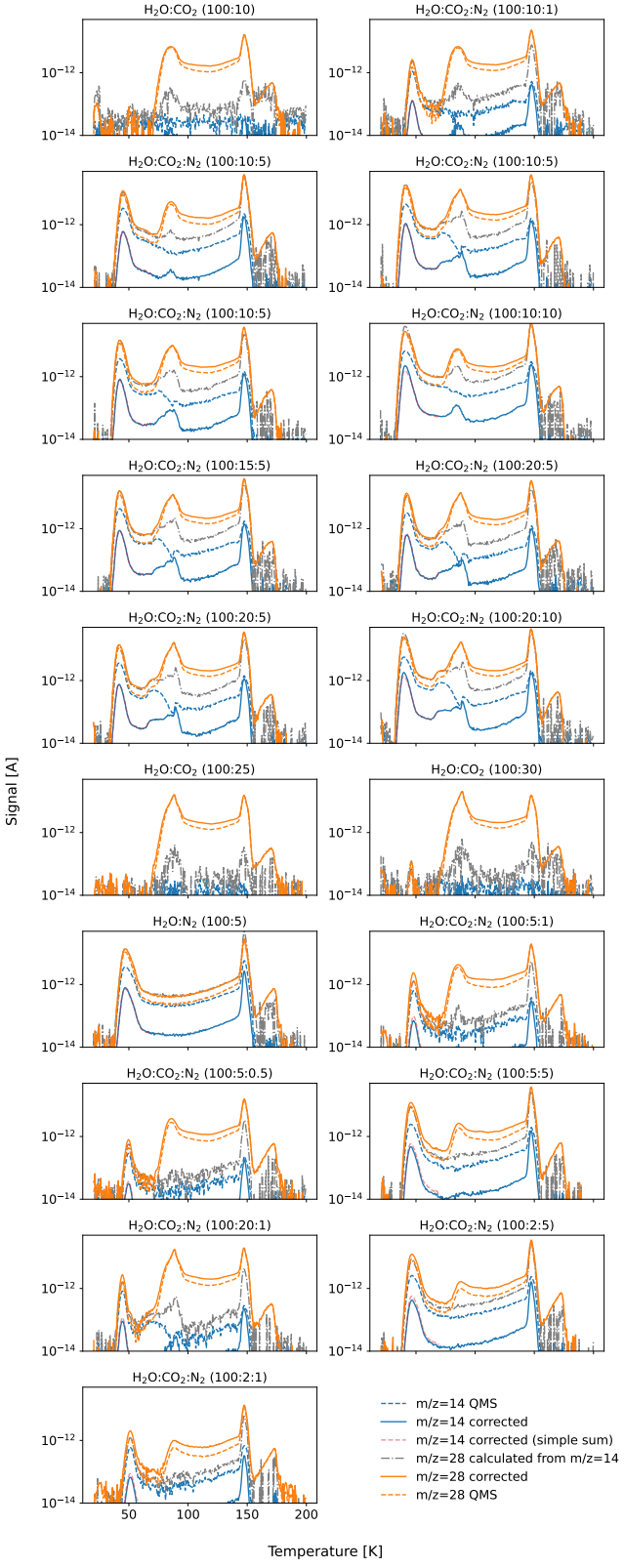

Fig. B.5. This figure shows the correction (described in Sect. 2.3) applied to all N_2 data (grey, dash-dotted). The m/z=28 signal consists out of contributions from both N_2 and CO_2, which necessitates the correction. Furthermore, a simple data correction has been performed, namely only summing the m/z=28 and m/z=14 signal and correcting for the expected fractionation pattern (red, dashed), which gives very similar results in the region where the only contribution to m/z=28 is N_2.

Appendix C: CO experiments

Analogous to Table 1 in the main text, the results from the CO ices are collected in Table C.1. TPDs of H_2O:CO_2:^{13}CO are shown in Fig. C.1. The H_2O:^{13}CO experiment has been excluded from the plot.

Table C.1. Fractions of ^{13}CO desorbing in the various integration regimes for the different ices.

Abundance in the Ice [with respect to water]			Total molecular abundance [%]			CO fraction desorbing		
H_2O	CO_2	^{13}CO	H_2O	CO_2	^{13}CO	Pure ^{13}CO desorption CO(CO peak) 30–60 K	Co-Desorption CO_2 CO(CO_2) 60–115 K	Combined H_2O release CO(H_2O) 115–200 K
100	0.19	2.24	97.63	0.18	2.19	0.313 ± 0.031	0.130 ± 0.026	0.554 ± 0.057
100	6.58	0.80	93.12	6.13	0.75	0.231 ± 0.035	0.132 ± 0.020	0.636 ± 0.054
100	13.58	0.90	87.35	11.86	0.79	0.259 ± 0.039	0.173 ± 0.017	0.566 ± 0.056
100	34.64	1.23	73.60	25.49	0.91	0.256 ± 0.038	0.329 ± 0.033	0.414 ± 0.071
100	7.61	4.08	89.54	6.81	3.65	0.341 ± 0.034	0.109 ± 0.016	0.548 ± 0.051
100	14.22	4.68	84.10	11.96	3.94	0.370 ± 0.037	0.182 ± 0.018	0.447 ± 0.055
100	25.40	4.23	77.14	19.59	3.27	0.296 ± 0.030	0.294 ± 0.029	0.408 ± 0.059

Notes. The regimes are referenced from Table 2 and the temperature limits of the integration have been added for convenience.

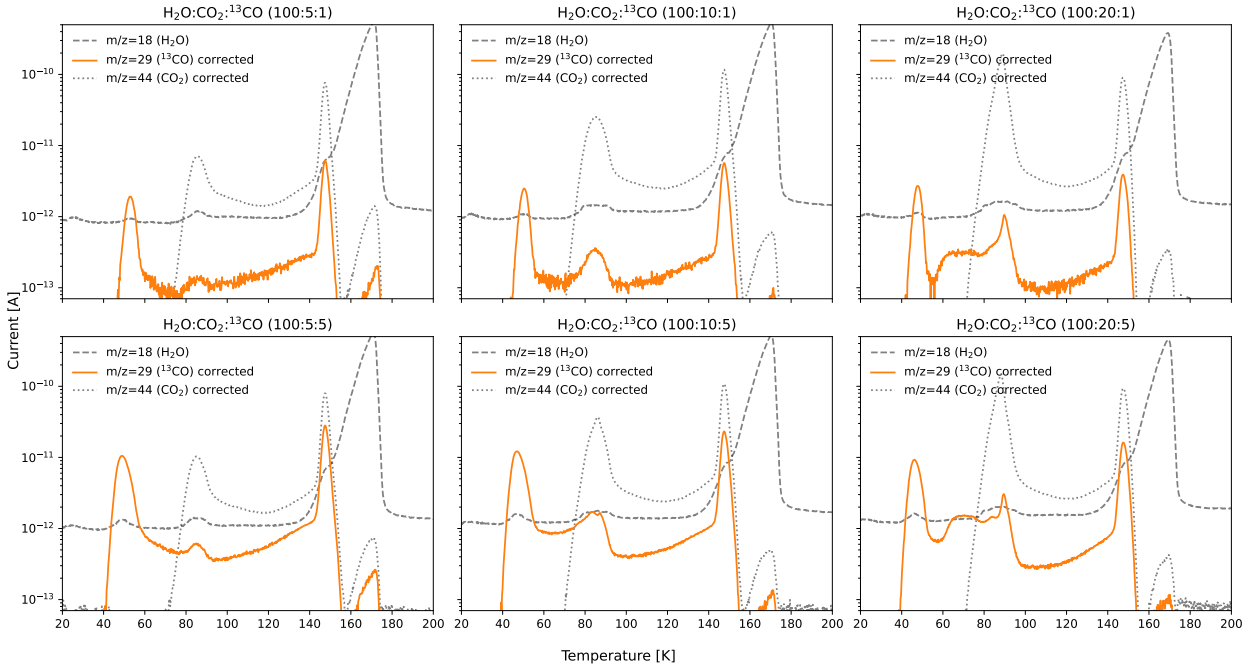

Fig. C.1. Desorption behaviour of m/z=29 (^{13}CO, orange), CO_2 (grey, dotted), and H_2O (grey, dashed). Both the ^{13}CO and CO_2 data have been corrected for the fractionation, for H_2O this was not necessary. The data was not baseline corrected for the display, but baseline subtraction was performed for further analysis. The figure titles correspond to the theoretical mixing ratio in the gas mixing system.

Appendix D: N_2 and ^{13}CO desorption plot

Figure D.1 shows the normalized desorption traces of N_2 and ^{13}CO as a function of temperature for all measured ices. It is an expanded version of Fig. 2 that contains all experiments shown in Tables 1 and C.1.

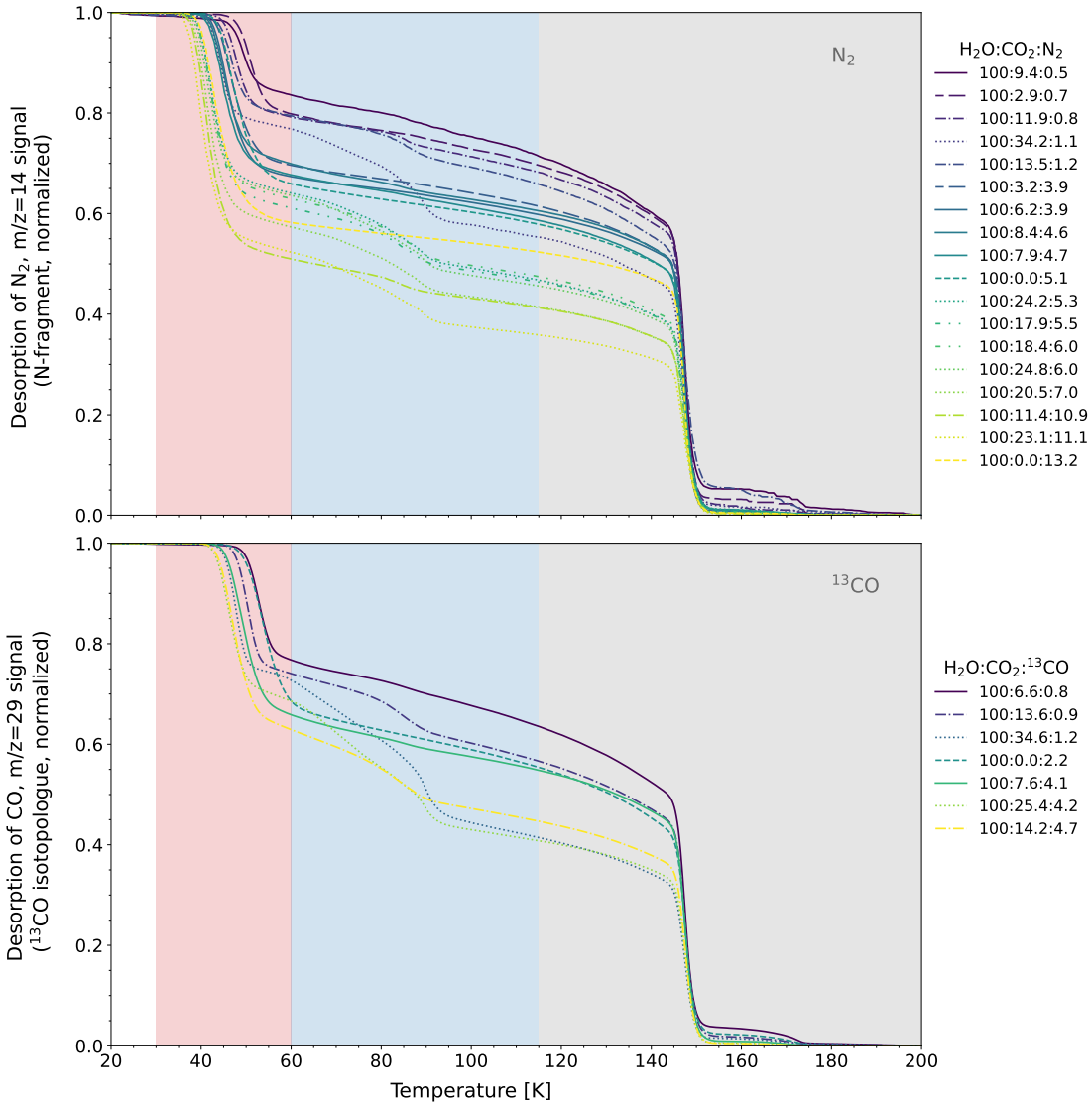

Fig. D.1. Plot showing the normalized desorption of N_2 and ^{13}CO as a function of temperature for all measured ices in Tables 1 and C.1.